MASTER THESIS

Calculation of Mechanical Stress of a Motorcycle Rear-frame

Carried out at

BMW Motorrad

in partial fulfilment of the requirements for the degree of Masters in

Computational Materials Science at the Technische Universität Bergakademie Freiberg

Under the Supervision and Guidance of

Prof. Dr. -Ing. Matthias Kröger, TU Freiberg

Dr. -Ing. Robert Szlosarek, TU Freiberg

By

Venkatasubramanian Sundaramoorthy

Masters in Computational Materials Science

Matriculation number: 64143

June 7, 2022

MASTER THESIS. DECLARATION OF AUTHORSHIP

I, Venkatasubramanian Sundaramoorthy, hereby declare that this thesis and the work presented in it are my own and have been generated based on my original research.

Further, I confirm that:

- This work was done mainly while in candidature for a master's degree in Computational Materials Science at the Technische Universität Bergakademie Freiberg;

- Wherever I have consulted the published work of others, the thesis is always clearly attributed;

- Where I have quoted from the work of others, the source is always given. Except for such quotations, this thesis is entirely my work;

- Wherever possible, I have redrawn or edited the graphs/diagrams using Microsoft PowerPoint, and the respective source is always mentioned;

- Where the thesis is based on work done by myself jointly with others, I have made clear precisely what others and what I have contributed myself;

"Hereby, I (we) formally declare that I (we) have developed and written the enclosed thesis without illegitimate help of a third party and that no other than the indicated aids have been used for its completion; all thoughts from other sources that have been used literally or indirectly are marked as such. The thesis has not been submitted to any other examination committee in this or a similar form."

Location: München

Date: June 7, 2022   *Venkatasubramanian Sundaramoorthy*

                                                                            Signature

ACKNOWLEDGEMENTS

Table of Contents

List of Figures

1.Introduction

Calculation of Mechanical Stress in Motorcycle Rear Frame is the main focus of the thesis. Design engineering is based on consecutive analysis, design and includes both over and under design. The material is selected according to the stress/strain characteristics of the individual parts. Products are inadequately designed to meet the needs of those who cannot afford more expensive alternatives. In terms of strength and durability, over-engineered components are beneficial. The rear structure must conform to real-world specifications without being overly complex. A complicated design is ineffective because it requires more effort and resources to build and construct than an efficient design. A high factor of safety (FOS) is now incorporated into the design of motorcycle rear frames, resulting in a heavier, more expensive product and material, labor, and monetary waste.

This study aims to optimize the design of a motorcycle's rear frame to reduce weight without affecting strength. The experimental setup for the analysis of rear frame vibration is recreated in the same circumstance as in the real world. The rear frame is subjected to a z-direction displacement load on the steering head and swingarm during experimental vibration research, while strain and acceleration output signals are recorded. The observed strain and acceleration signals are used to determine how accurately the simulated data represents reality. Occasionally, a steering head or swing arm receives an input signal with a low amplitude. However, the output signal, such as acceleration, responds unexpectedly, which raises the question of whether the higher and lower amplitudes of the acceleration signal result from a material response or input signal. The unpredictability of the acceleration signal's results must be analyzed in the time and frequency domains.

The rear frame is simulated in the same manner as the experimental arrangement, with the Abaqus amplitude curve used to specify the time-displacement signal in the steering head and swingarm. The simulated acceleration signal with time displacement on the swingarm and steering head does not match the experimentally determined acceleration data. As a result, the rear frame is expanded with a mass-spring system employing a connector element to recreate the driver and rear position mass in experimental analysis. The mass-spring coefficients are chosen according to how closely the simulated and experimental acceleration data match.

The rear frame is designed using Abaqus, a shell structure, and a vibration boundary condition. The rear frame was subjected to an experimental vibration study, generating strain and acceleration signal data. In MATLAB, these signals are evaluated in the time-frequency domain using the Short-time Fourier Transform, the critical time points are retrieved, and critical stresses are calculated using the Dynamic implicit technique. A spring-mass system was developed to validate simulation and experimental results using the Abaqus connector element. By conducting a parametric analysis with varying spring, mass, and damping coefficients, the influence of spring and damping coefficients on the acceleration signal is determined. As a result of the parametric analysis, the critical stresses are estimated in Abaqus using the appropriate connector coefficients. These stresses serve as the basis for determining a structure's durability and deterioration. The experimental results are utilized to verify the simulation results.

2 Theoretical Background

The analysis of sound and vibration signals is becoming more complicated. Time and frequency are the most fundamental variables in Signal Processing. Key variables in the time and frequency domains are retrieved to accurately represent the characteristics of a signal during characterization. Several techniques exist for extracting vibrational features; early research on vibration signal processing relied heavily on time series (Heng, 1998), frequency domain (Brie, 2000), and time-frequency domain analysis (Mori, 1996) (Gao, 2006).

2.1 Time domain Analysis

Combining sound and vibration information, time-domain analysis (Heng, 1998) implemented quantitative analysis to evaluate the presence of flaws in bearings. Utilizing statistical study to monitor production processes and machine circumstances. Statistical properties such as RMS[1], crest factor[2], and kurtosis[3] are examined to identify the bearing defect.

---

[1] RMS: The root mean square of a signal calculates the signal's mean value over time. It represents the average signal "power."
[2] Crest Factor: The crest factor corresponds to the peak amplitude of a waveform divided by its root-mean-square (RMS) value; it represents the severity of a waveform's peaks.
[3] Kurtosis: It is a statistical parameter that measures the 'peakiness' of a signal to characterize it.

2.2 Frequency domain Analysis

Processing of vibration signals in the frequency domain (Brie, 2000), This paper investigates the spalled bearing vibration model and conventional techniques and the constraints of time-frequency experimental data signals. Figure 1(a) depicts the vibration signals produced by a defect in the inner race of the drive shaft ball bearing. Imperfections in the time domain signal generate transients with particular resonance, but their structures vary considerably. Figure 1(b) depicts the amplitude spectrum of the vibration, which contains numerous spectral lines over a broad frequency range. If the defect is minor, the gear signal can compensate for the bearing's contribution. The impact of load distribution and an approximation of the contact angle are two crucial factors that complicate the study. Utilizing time-frequency vibration analysis helps overcome the limitations of both temporal domain and frequency analysis.
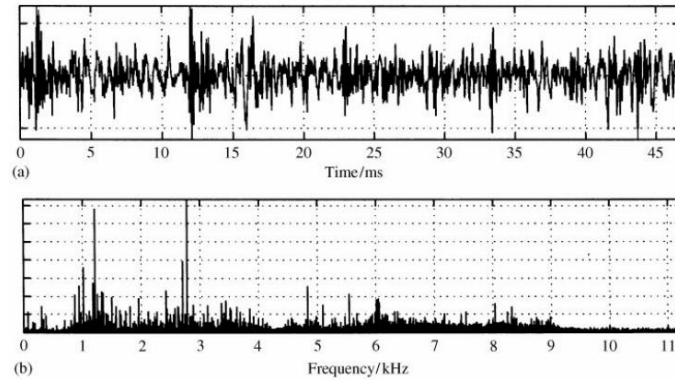
Figure 1: Single point defect bearing vibration signal analysis (Brie, 2000) (a) time domain vibration signal (b) amplitude spectrum

This investigation demonstrated the effectiveness of time-frequency techniques by highlighting the problems associated with traditional models.

2.3 Time Frequency Analysis

The main focus of time-frequency analysis is to identify and describe instances in which the frequency information of a signal varies over time. The discrete wavelet transform (DWT) is applied to vibration analysis in time-frequency domain analysis (Mori, 1996) by analyzing accelerometer readings to detect spalling in rolling elements. DWT provides the temporal and frequency characteristics of the input

signal. By dividing the wavelet function, the discrete Wavelet Transform (DWT) is derived from the Continuous Wavelet Transform (WT) and is suitable for its computational simplicity. The difficulty in identifying impulsive actions is because the amplitude of the sudden force is small and therefore easily concealed by other vibrational events. Since impulsive reactions span a wide frequency range, the Fast Fourier Transform (FFT) is no longer used. During these impulsive reactions, the wavelet coefficients increase in value as the frequency of spalling increases. Spalling can be predicted by observing the trend of the values of the maximal wavelet coefficients.

The short-time Fourier Transform is the most common method in time-frequency analysis for representing stationary and non-stationary signals (STFT). Stationary signals have statistical properties independent of time, such as mean value and autocorrelation. Traditionally, spectral techniques, such as the Fourier Transform, which detects the frequency components of a signal, have been used extensively to study stationary signals (Gao, 2006). The Fourier transform is rendered ineffective because of the statistical characteristics of a non-stationary signal change over time. The following are the three fundamental components of non-stationary signals observed in industrial machinery (Gao, 2006):

1. Periodic components result from the cyclical interactions of the machine's components.

2. Transient elements are induced by "specific time" events, such as the fracture of a drill bit or a crack initiation within the workpiece.

3. Sounds in the background.

Due to the inherent short duration and low magnitude of transient signals, precise detection has remained challenging.

Comparative analysis of temporal frequency analysis methods for non-stationary signal analysis in bearing health monitoring is presented (Gao, 2006). Examining the capability of the short-time Fourier transform (STFT), the wavelet transform (WT), the wavelet packet transform (WPT), and the Hilbert-Huang transform (HHT) to detect features in time-varying events. The waveform of vibration obtained from a ball bearing with a localized defect is depicted in Figure 2a. Figure 2b

displays the five major frequency components at 40, 250, 1000, 1200, and 1500 Hz, but not their temporal variations.
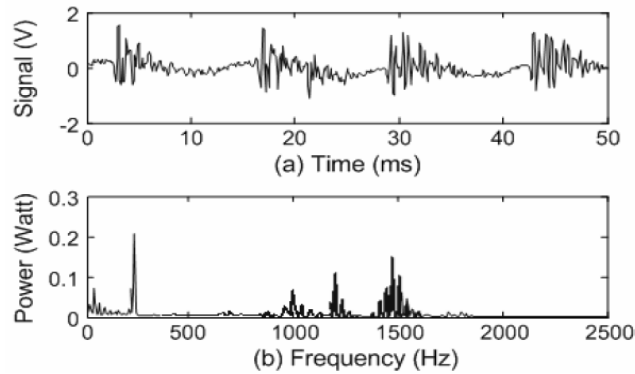
Figure 2: Bearing vibration signal and its spectrum (Gao, 2006)

Figure 3 demonstrates that one of the frequency components shifted from 1200 to 1000Hz at a time point of 20ms when the same signals were analyzed using the Short-time Fourier Transform (STFT) with a 12.8ms window. This indicates that the frequency change along the timeline can be utilized to show the bearing defect's progression.
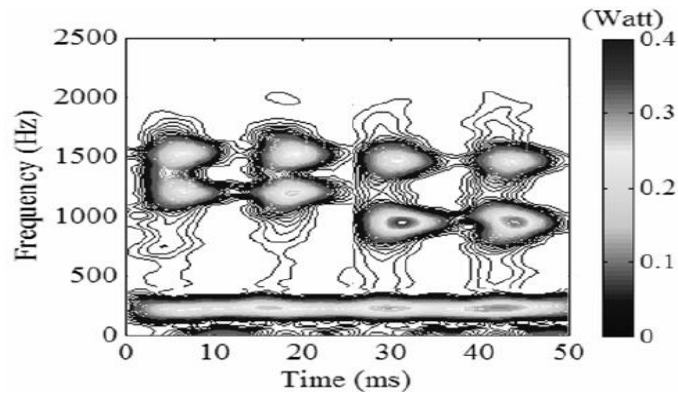
Figure 3:STFT of bearing vibration signal (Gao, 2006)

2.3.1 Short-time Fourier Transform (STFT)

The short-time Fourier Transform is built on the concept that when you want to determine which frequencies exist at a particular time, you should analyze a small portion of the signal while ignoring the rest. Figure 4 demonstrates that STFT sequentially performs a 'time-localized' Fourier transform of the signal x(t) using a sliding window function g(t) centered at a time, and the results display the frequency variation of the signal as time progresses.
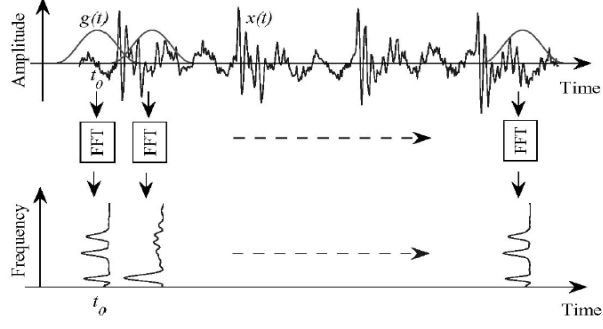
Note: FFT-Fast Fourier Transform

Figure 4:Illustration of Short-time Fourier Transform of a test signal (Gao, 2006)

Mathematically, STFT is defined as,

$$STFT(\tau, f) = \int x(t)g(t-\tau)e^{-j2\pi ft}dt = \int x(t)\dot{g}_{\tau,f}(t)dt \text{ (Gao, 2006)} \qquad 1.1$$

Where $(*)$ represents the conjugate complex of the function. The window function directly influences the time and frequency resolution of signal decomposition.

The selection of Window and overlap parameters must be taken into account for STFT signal analysis.

The time and frequency resolutions of the window function are affected by the window size. Figure 5 depicts the effect of window size on time and frequency resolution when STFT with a Gaussian window was applied to the signal in Figure 4 with four different window sizes: 3.2, 6.4, 12.8, and 25.6 ms.
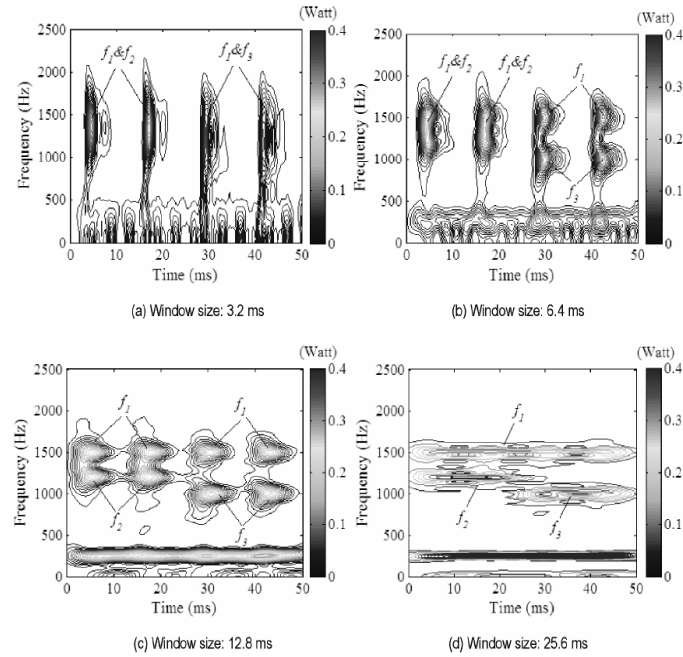

Figure 5:Results of STFT of the test signal using four different window sizes (Gao, 2006)

6

In Figure 5(a), the smallest window of 3.2 milliseconds had a time resolution, which was sufficient for separating the four pulse trains contained in the signal; however, the frequency resolution was insufficient. The largest possible window size of 25.6 milliseconds offers a frequency resolution that is good enough to identify the three-frequency component shown in Figure 5(d). On the time-frequency plane, as shown in Figure 5(c), all pulses can be differentiated to a sufficient degree when using a window size of 12.8 milliseconds.

2.3.2 Wavelet Transform (WT)

Unlike the STFT, which has a fixed window size, the wavelet transform permits variable window sizes when examining different frequency components of a signal. Large windows for low frequencies and small windows for high frequencies. In contrast to the Fourier Transform, which represents a signal as the sum of a sequence of sine and cosine functions with a single frequency, the wavelet transform decomposes a signal into a set of functions derived by scaling[4] and shift[5] the mother wavelet. Definition of the wavelet transform of a signal $x(t)$ is defined as,

$$WT(s, \tau) = \frac{1}{\sqrt{s}} \int x(t) \dot{\psi} \left(\frac{t - \tau}{s} \right) dt \text{ (Gao, 2006)} \qquad 1.2$$

τ is the shifting parameter, where s>0 indicates the scaling parameter that affects the time and frequency resolutions. $\dot{\psi}$ represents the complex conjugation of the mother wavelet $\psi(t)$ and its scaled version is expressed as.

$$\psi(t) = \exp(i2\pi f_0 t) \exp(-\alpha t^2 / \beta) \text{ (Gao, 2006)} \qquad 1.3$$

$$\psi[(t - \tau)/s] = \exp[i2\pi f_0 (t - \tau)/s] \exp[-\alpha (t - \tau)^2 / s^2 \beta^2] \text{ (Gao, 2006)} \qquad 1.4$$

With f_0, α, β are constants. Morlet wavelet time and frequency resolutions are computed, suggesting that time and frequency resolutions are proportional to scaling parameter s both directly and indirectly.

A pair of low-pass and high-pass wavelet filters, designated $h(k)$ and $g(k) = (-1)^k h(1 - k)$ respectively, can efficiently perform Discrete Wavelet Transform

---

[4] Scaling: the smaller the scale factor, the more "compressed" the wavelet, and the greater the scale factor, the more extensible.
[5] Shifting: delaying or advancing a wavelet

(DWT) signal decomposition. The selected mother wavelet $\psi(t)$ and its associated scaling function $\varphi(t)$ are as follows:

$$\varphi(t) = \sqrt{2} \sum_k h(k)\varphi(2t-k) \text{ (Gao, 2006)} \qquad 1.5$$

$$\psi(t) = \sqrt{2} \sum_k g(k)\varphi(2t-k) \text{ (Gao, 2006)} \qquad 1.6$$

The signal is divided into four levels after passing through the first level's high pass and low pass filters. The output of the low pass filter is subjected to the second level of filtering. Repeat the procedure until the test signal has been decomposed after the fourth level of decomposition.

The findings of a four-level decomposition of the test signal using six mother wavelets demonstrate that the type of mother wavelet employed directly affects the efficiency of transient element detection. In contrast to the STFT, the discrete wavelet transform provides adjustable time-frequency resolution; nevertheless, it has a relatively low resolution in the high-frequency domain, making it challenging to discern high-frequency transients.

2.3.3 Wavelet packet Transform (WPT)

Compared to the discrete wavelet transform, the Wavelet Packet Transform (WPT) significantly decomposes the detailed information in the high-frequency range of the signal, so it eliminates its drawback. The following functions are required to accomplish the wavelet packet transform of a signal after four layers of decomposition:

$$u_{2n}(t) = \sqrt{2} \sum_k h(k)u_n(2t-k) \text{ (Gao, 2006)} \qquad 1.7$$

$$u_{2n+1}(t) = \sqrt{2} \sum_k g(k)u_n(2t-k) \text{ (Gao, 2006)} \qquad 1.8$$

Where $u_0(t) = \varphi(t)$ and $u_1(t) = \psi(t)$. Due to its enhanced signal decomposition capacity, WPT is an intriguing tool for detecting and discriminating high-frequency transient features. There are several methods for analyzing the signal, allowing you to optimize and enhance the process. If the higher level has returned less entropy than the sum of the entropies at the lower level, then the sub-frequency band at the upper level will be kept. The inverse connection between entropy and energy concentration can be utilized to differentiate transient elements in the sub-frequency band. As shown in

Figure 6, a wavelet packet transform employing the minimum entropy approach was used to identify and discriminate all eight transient elements in the signal.
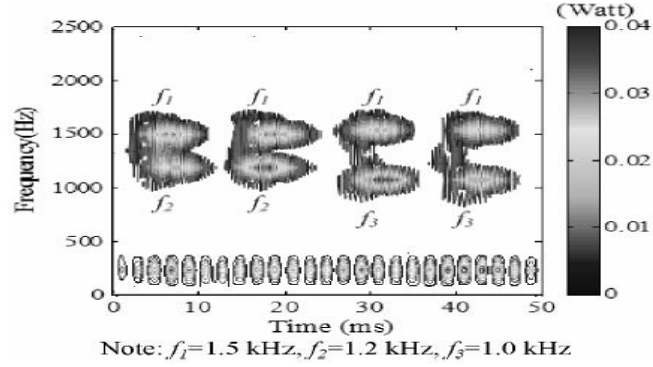

Note: f_1=1.5 kHz, f_2=1.2 kHz, f_3=1.0 kHz

Figure 6:Wavelet Packet Transform of a test signal (Gao, 2006)

This suggests that, for non-stationary signals, wavelet packet transform outperforms discrete wavelet transform.

2.3.4 Hilbert-Huang Transform (HHT)

The Hilbert Huang Transform (HHT) is a technique for evaluating time frequency that combines the Empirical Mode Decomposition (EMD) and the Hilbert Transform. Assuming that the subject signal is present,

1. At least two extreme values

2. To possess a time scale distinguished by the time delay between successive changes in local peak position

3. When no extrema are present, the inflection points remain and can be distinguished multiple times to reveal the extrema.

HHT empirically decomposes the signal into Intrinsic Mode Functions (IMFs). Each IMF defines the distance between the signal and the average envelope values.

The empirical mode decomposition procedure for the signal $x(t)$ is detailed below,

$$x(t) = \sum_{i=1}^{n} c_i(t) + r_n(t) \text{ (Gao, 2006)} \qquad 1.9$$

The IMF Hilbert transform $c_i(t)$ is written as $c_i(t)$ is the ith IMF of the signal and r_n is the residue

$$H[c_i(t)] = \frac{1}{\pi} \int \frac{c_i(\tau)}{t - \tau} d\tau \text{ (Gao, 2006)} \qquad\qquad 1.10$$

Because $c_i(t)$ is the real component of an analytic signal $z_i(t)$ and r_n is disregarded, the expression could be modified as follows:

$$x(t) = \text{R} \left[\sum_{i=1}^{n} \alpha_i(t, \omega_i) e^{j \int \omega_i(t) dt} \right] \text{ (Gao, 2006)} \qquad\qquad 1.11$$

Where R is the real component of the signal and at time t with frequency ω_i the amplitude of the i$^{\text{th}}$ IMF is $\alpha_i(t, \omega_i)$

HHT of the signal $x(t)$

$$HHT(t, \omega) = \sum_{i=1}^{n} \alpha_i(t, \omega_i) \text{ (Gao, 2006)} \qquad\qquad 1.12$$

The HHT is a valuable approach for non-stationary signal analysis due to its time-varying amplitude and instantaneous frequency. Figure 7(a) depicts the HHT and intrinsic mode functions (IMF) of the test signal, and Figure 7(b) illustrates the Hilbert-Huang spectrum (b).

(a) IMF extracted from the signal   (b) Hilbert-Huang spectrum of the signal
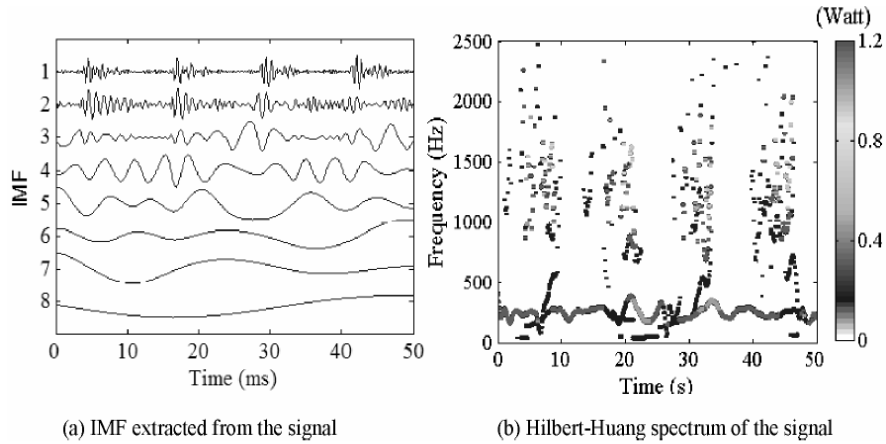
Figure 7:HHT of a test signal (Gao, 2006)

While the four sets of instantaneous elements in the test signal $x(t)$ were distinguishable along the temporal axis, time overlay excitations could not be separated along the frequency axis.

The effectiveness of STFT, DWT, WPT, and HHT was investigated using ball-bearing vibrations. Consequently, using a Short-time Fourier Transform with sufficient window size, the frequency changes associated with the propagation of bearing faults were observed. It has been demonstrated that the wavelet packet transform can identify all transient elements in both the mathematically created test signal x(t) and the

vibration data observed from the bearing. In contrast, the DWT and the HHT failed to identify. Based on the findings of the research publication, STFT is the most extensively used method in time-frequency analysis for stationary and nonstationary signals, as it identifies transient signals with the correct window size.

3. Experimental and Simulation setup
3.1 Experimental setup

The rear frame is loaded in the z-direction on the steering head and swingarm for approximately 260 seconds using time-displacement signals during the vibration analysis. Figure 8 displays the experimental setup.
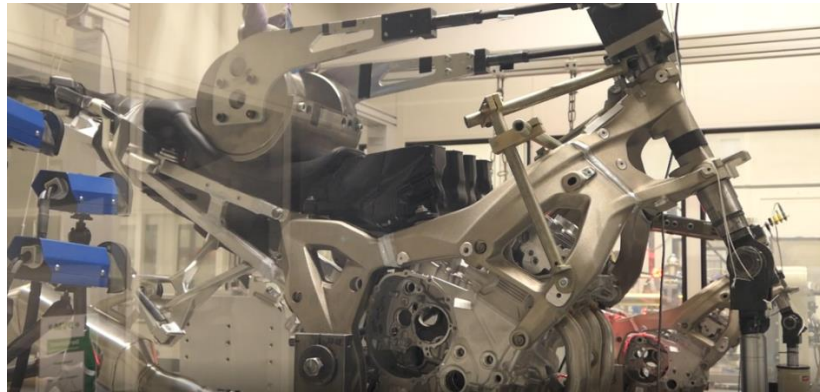
Figure 8:Experimental setup of the vibration analysis

The displacement in the z-direction is applied to the steering head and swingarm via the hydraulic cylinders using time-displacement signals, as shown in the diagram, and the output data as strain and acceleration signals in the z-direction are obtained from the rear frame using strain gauges on both side (right and left side of the rear frame) and accelerometers. These strain signals are received using strain gauges positioned in a specific manner within the rear frame.

Similarly, the accelerometer is mounted in the same way during testing under actual road conditions. The accelerometer and strain gauge position in the experimental setup is shown in Figures 9(a) and (b). A cylindrical mass on the driver's and passenger's seats rises and falls relative to the temporal displacement signals. Steering head and swing arm time-displacement signals are necessary to execute the simulation.

(a): Location of accelerometer in the experimental setup

(b): Location of the strain gauge in the experimental setup

Figure 9: (a) Location of accelerometer, (b) Location of Strain gauge in the experimental setup

As depicted in Figure 9(b), strain gauges are installed on both sides of the rear frame. Acceleration data corresponding to the simulation and experimental data are generated and then utilized to determine the degree of correspondence between the two data sets.
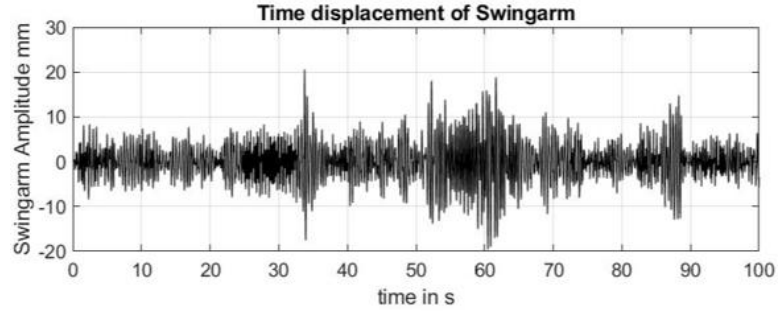
3.2 Simulation and Time displacement signal
3.2.1 Time displacement signal

Figures 10 (a) and (b) depict the z-direction displacement signal for 100s in the steering head and swingarm, respectively, while Figure 10(c) illustrates the acceleration signal from the accelerometer in the rear frame for 100s.
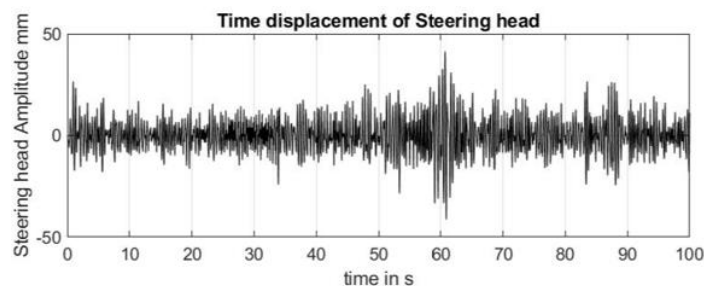
(a): Time displacement signal of Steering head

(b): Time displacement signal of swing arm
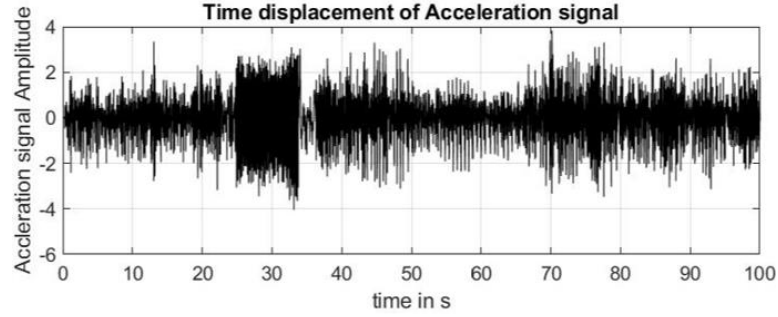
(c): Acceleration data from the rear frame vibration analysis

Figure 10: Time displacement signal of (a) Steering head, (b) Swingarm and (c) acceleration data

At 55s, the steering head and swingarm displacements are high amplitude, but the accompanying acceleration signal is relatively moderate compared to other time points. Therefore, it is unclear how the acceleration signal responds to the steering head and swingarm time displacement signals.

Time domain, frequency domain, and time-frequency analysis are done to comprehend the signal's characteristics. Only static features, such as minimum, maximum, and mean values, are recovered in the time-domain study, not revealing the signal's properties. Figure 11(a) and Figure 11(b) depict the results of applying Fourier Transform to the steering head and swingarm displacement signals in frequency domain analysis.
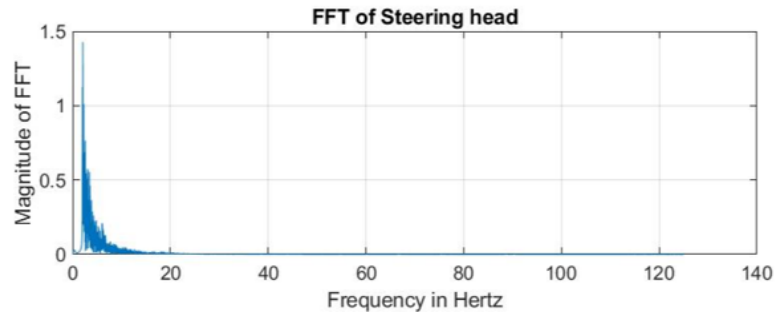

(a): Fourier Transform of steering head
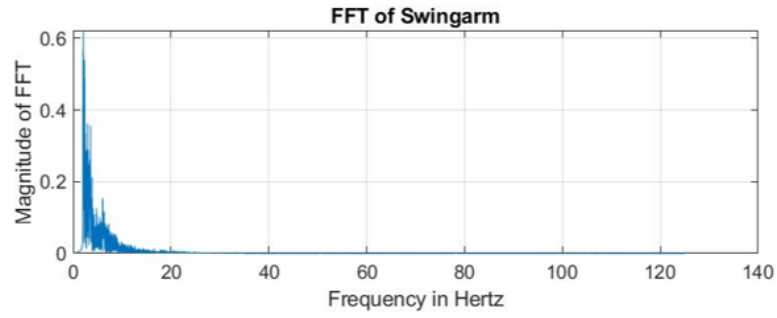
(b): Fourier Transform of swing arm

Figure 11: Fourier Transform of (a) Swing arm, (b) Steering head signal

The preceding graphs indicate that the dominating frequencies are present, but the corresponding temporal resolution is obscured. The purpose of time-frequency analysis is to determine the frequency and temporal resolutions. According to a study by Gao (2006), both STFT and WPT can identify transitory signals. Short-time Fourier Transform is the most used technique for time-frequency analysis, and it is applied to all signals; the outcomes are detailed in the section under "Results."

The window type and overlap parameters must be considered for short-time Fourier analysis. The Window is the duration of time during which a signal is evaluated, as described in Appendix 1. Various window functions are implementable based on the signal. Each Window possesses distinctive qualities and is suitable for several applications. Figure 12 (a), (b), and (c) demonstrate the outcomes of applying rectangular Window, hamming Window, and gaussian Window to the signal depicted in Figure 10 (b), respectively.
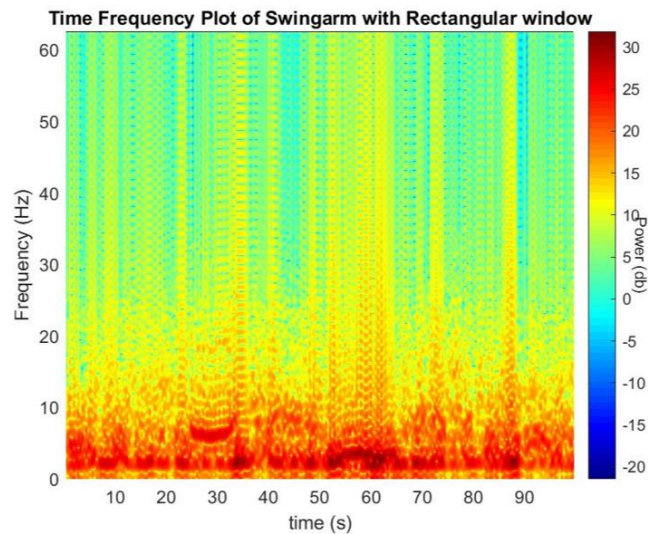
(a): Swingarm signal using STFT and Rectangular window

14
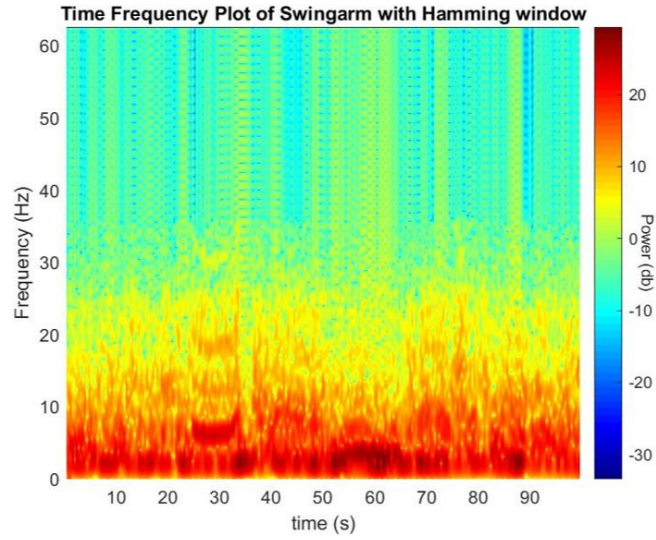
(b): Swingarm signal using STFT and Hamming window
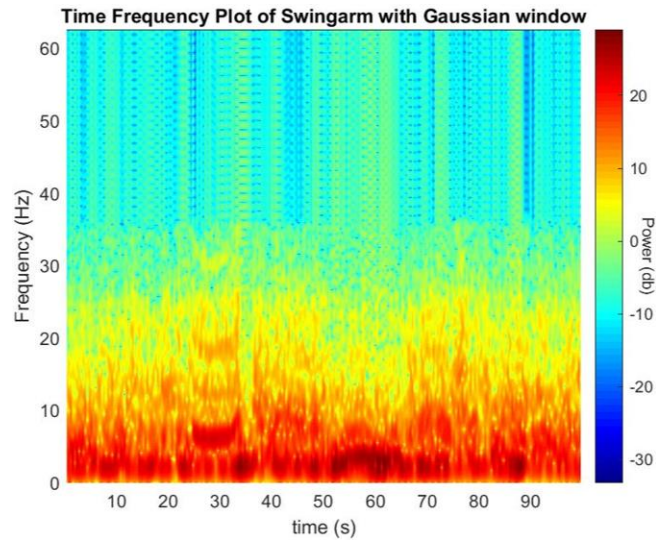
(c): Swingarm signal using STFT and Gaussian window

Figure 12: STFT signal analysis of Swingarm with (a) Rectangular, (b) Hamming and (c) Gaussian window

As demonstrated by prior research, a rectangular window is suitable for distinguishing signals with identical frequency and strength. Temporal and frequency resolutions are not distinguishable in the Gaussian frame. The Hamming window provides a more accurate depiction of the signal's frequency spectrum.

Window functions $g(t)$ are tapered in both corners, resulting in signal leakage when applied to a signal. Figure 13 depicts the leaking and overlap. Typically, a 50 percent overlap is used to prevent leakage by implementing overlap parameters.
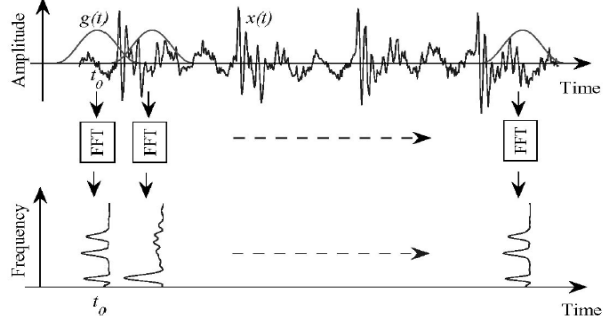
Note: FFT-Fast Fourier Transform

Figure 13:Window function g(t) with overlap (Gao, 2006)

The sizes of the windows are chosen through trial and error. As shown in Figures, 14 (a) and (b), a smaller window yields a higher temporal resolution, whereas a larger size yields a higher frequency resolution for the signal displayed in Figure 10(b) is subject to Hamming window.
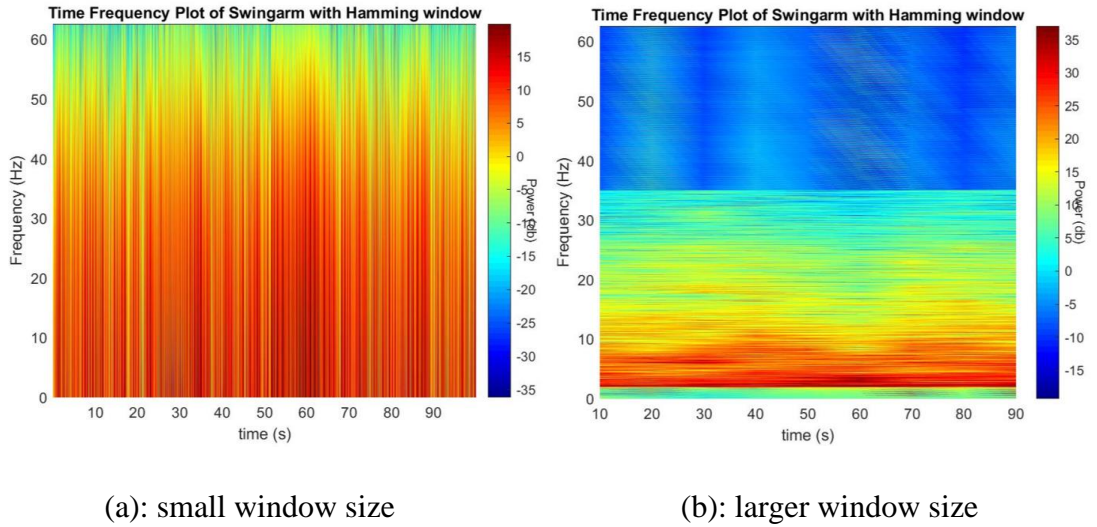

(a): small window size   (b): larger window size

Figure 14: Hamming window with (a) small, (b) large window size

The steering head and swingarm time displacement signals are evaluated utilizing a hamming window with appropriate window size and a 50% overlap parameter, and the results are provided in the section labeled Results.

3.2.2 Simulation setup

As shown in Figure 15, the rear frame is constructed using a shell structure and vibration boundary conditions using Abaqus. Moreover, the temporal displacement targets are applied in the steering head and swingarm, as demonstrated below:
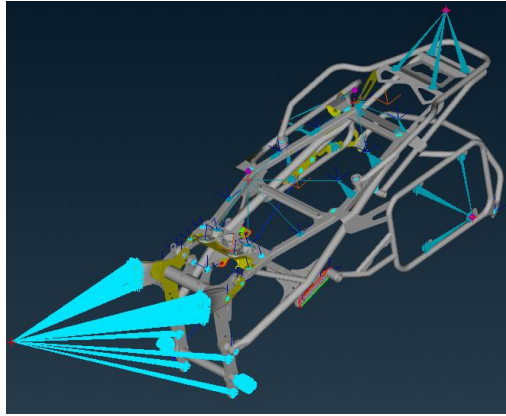
16

Figure 15:Rear frame with shell structure and vibration boundary condition

The time and displacement given signal values of the steering head and swingarm are viewed in Tecware, and the signals are extracted using Python script; Figure 16 (a) depicts the signal points in Tecware, and Figure 16 (b) illustrates how the signal is implemented in Abaqus utilizing an Amplitude curve.
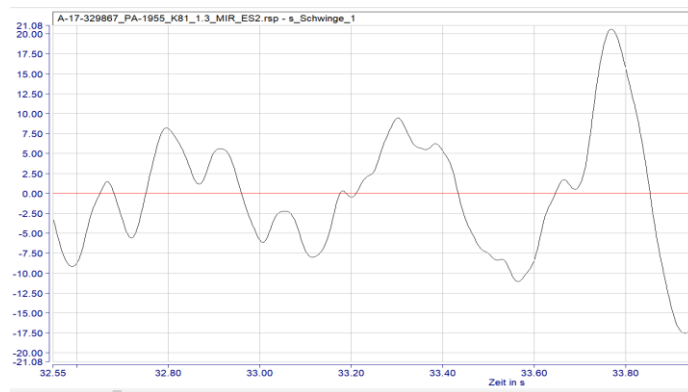
(a): Time displacement signal of Swing arm in Tecware
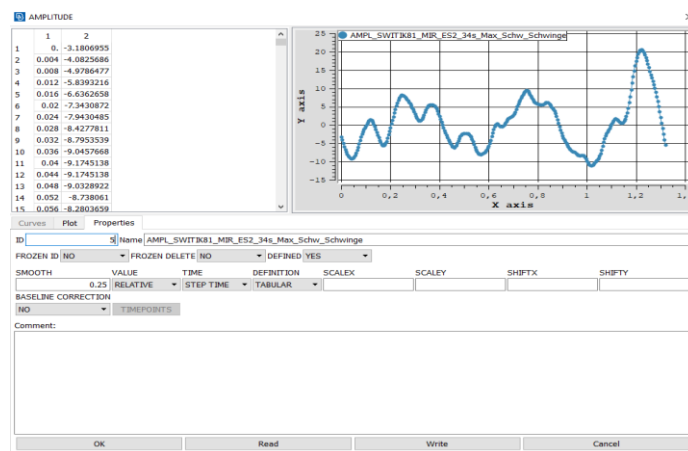
(b): Time displacement signal of Swingarm in Abaqus using Amplitude curve

Figure 16: Time displacement of swingarm signal in (a) Tecware and (b) Abaqus

The simulation steps comprise ten seconds of gravity force and one second of the steering head and swingarm time-displacement signal. In the simulation, the spatial acceleration[6] is measured at the precise location of the experimental accelerometer. Figure 17 illustrates the spatial acceleration in the back frame, as same as the location of accelerometer in the experimental setup shown in Figure 10(b).
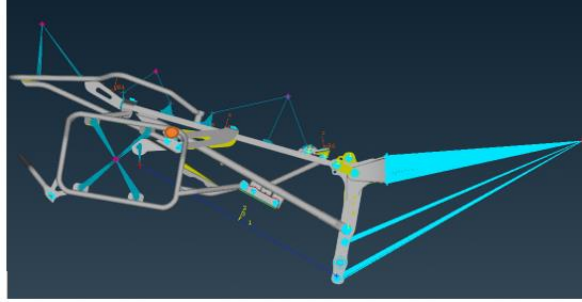

Figure 17: Location of the spatial acceleration in the simulation

As shown in Figure 18, the simulation was performed with a stiff mass on the driver, the back, the luggage, and the top case.
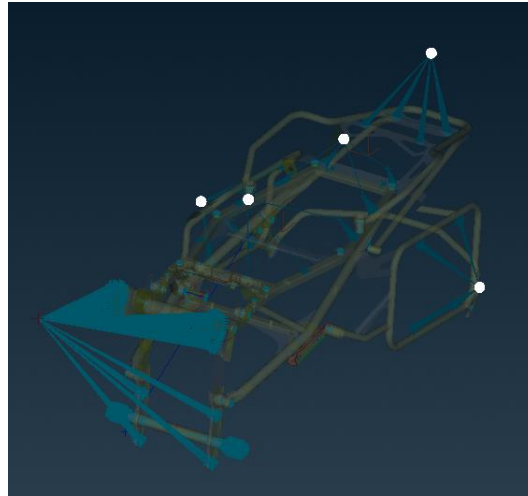
Figure 18: Rigid mass on Driver, back, luggage and top case

The simulation's acceleration data is compared to the experiment's acceleration data. The simulation data with time displacement signal and acceleration were computed assuming the mass was fixed. The mass on the driver and rear position is fixed to the rear frame and moves up and down. Figure 19 depicts simulation and

---

[6] Spatial Acceleration: The acceleration value is measured at a fixed location.

experiment results on acceleration for the time displacement signal shown in Figure 16 (b).
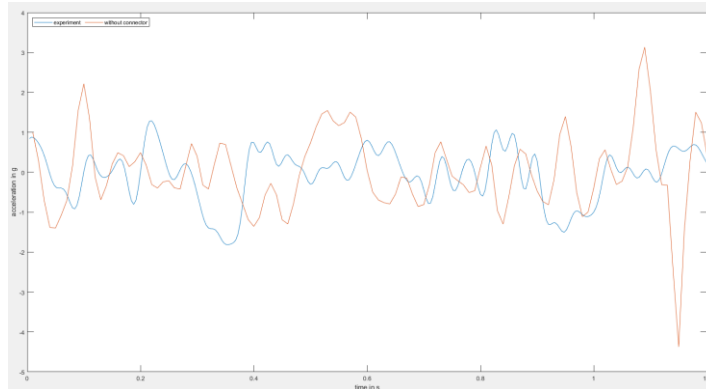

Figure 19: Experiment and simulation acceleration data

The stiff mass is significant for the mismatch between the simulated and experimental acceleration measurements. The driver and rear position mass are not rigidly linked to the rear frame in a realistic condition. Consequently, the rigid mass must be modeled in Abaqus with a spring and damper using the connector element.

3.2.2 Connector Modeling:

It includes the correct connector parts, the behavior of the connectors, connector activation, and output monitoring. It can specify a link between two nodes (each node can be connected to a rigid part, a deformable part, or not linked to any part). Using this property correctly, a link between a node and a ground can be defined. Connector elements can be employed for two-dimensional analysis, axisymmetric studies, and three-dimensional investigations. There are two types of connector elements, 2D and 3D, and the kind must be chosen dependent on the dimension of the analysis being performed. Connector elements are limited to two nodes, and the behavior of the first node determines the position and motion of the second node. Connector elements have relative displacements and rotations local to the component; this is known as the component's relative motion. Relative motion components may be limited or uncontrolled depending on how the connector element is defined. Translations and rotations are the components of relative movement that are restricted by the connection element. The available components of relative motion are displacements and rotations that are not kinetically restricted and are therefore

available for describing material-like behavior and specifying time-dependent motion. The connector's behavior can be determined for connection types with available relative motion components. It is possible to incorporate specific applications, such as the simple spring, dashpot, and node-to-node contact. For unconstrained relative motion components, it may comprise linear or non-linear force versus displacement and force versus velocity behavior. It allows for modeling spring-like elastic behavior, rigid-like elastic behavior. Only the available components of relative motion can be employed to characterize kinetic behavior. Assembled connections, complicated connections, translation connections, rotational connections, and specialized translation basic connections are the various sorts of connectors.

1) Translation fundamental connection: It influence translation degrees of freedom at both nodes and, perhaps, rotational degrees of freedom at the first node or both nodes on the connector element.

2) Rotational basic connection: It affects just rotational degrees of freedom at both connector nodes.

3) Specialized rotational basic connection: impact, in addition to the rotating degree of freedom, other degrees of freedom at the nodes of the connector element.

4) Assembled connections: preconfigured translation and rotation or translation and specialized rotational essential connection elements

5) Complex connection: impacts the degree of freedom combination at the connector element's nodes and cannot be mixed with other connected components.

The driver, rear, luggage, and top case positions shift transversely with the rear frame of the experimental arrangement. In the simulation, translational connection elements replace the masses. Over the various forms of translation connectors, axial and cartesian type connectors are researched based on the direction of movement in the vibration setup.

Axial connector: Figure 20 demonstrates the axial connector. It establishes a link between two nodes whose relative displacement is along the line separating them. Axial connectors have separate physical connections, such as springs, axial dashpots, and gap-like contacts.
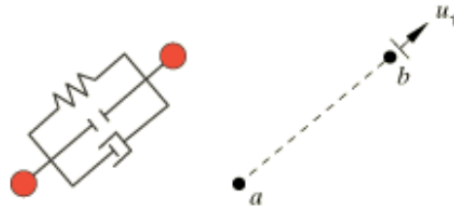
Figure 20: Axial Connector

The axial connector does not restrict any component of relative motion; the available component of relative motion, u1, acts along the line connecting the two nodes; rotational degrees of freedom are not activated for the axial connector. As indicated in Figure 21, the axial connector's available component and connection type are presented.

Figure 21: Summary of Axial connector

Cartesian connector: It provides the connection between two nodes in which the change in position for node an is measured in three local connection directions. Figure 22 illustrates the Cartesian connector type.
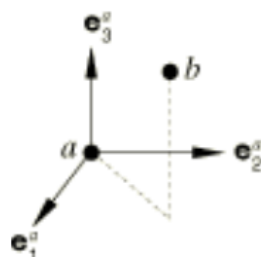
Figure 22: Cartesian connector

This sort of connector does not impose kinematic limitations. It identifies three local directions {e_1^a, e_2^a, e_3^a} at node a and measures the positional changes of node b along with these local coordinates. As seen in Figure 23, the available components of relative motion are the u1, u2, and u3 directions.

CARTESIAN

Basic, assembled, or complex:	Basic
Kinematic constraints:	None
Constraint force output:	None
Available components:	u_1, u_2, u_3
Kinetic force output:	f_1, f_2, f_3
Orientation at *a*:	Optional
Orientation at *b*:	Ignored
Connector stops:	$l_1^{min} \leq x \leq l_1^{max},$
	$l_2^{min} \leq y \leq l_2^{max},$
	$l_3^{min} \leq z \leq l_3^{max}$
Constitutive reference lengths:	$l_1^{ref}, l_2^{ref}, l_3^{ref}$
Predefined friction parameters:	None
Contact force for predefined friction:	None

Figure 23: Summary of Cartesian connector

Figure 24 depicts the experimental setup with masses and the transverse movement of the mass with the rear frame. In addition, the masses are connected to a hydraulic cylinder near the steering head, which raises and lowers the masses. One-directional relative motion is provided and can be substituted by an axial connector.
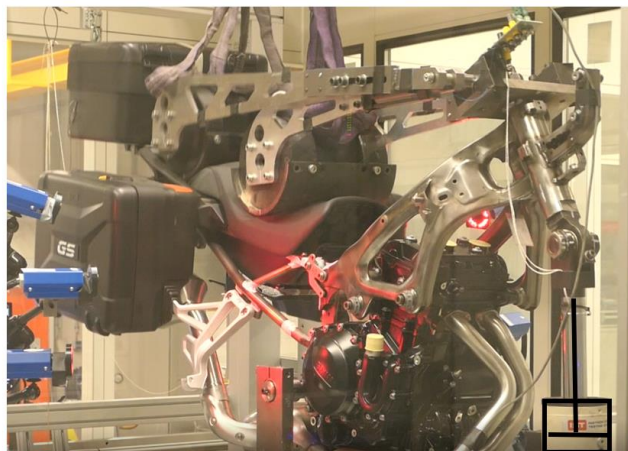
Figure 24: Translation movement of masses

In the driver position of the simulation model with a given spring and damping coefficient, an axial connector with mass, spring, and damping coefficient is introduced. With initial spring and damping coefficients for the connector element in the driver position, the vibration signal in the swing arm depicted in Figure 16 (b) is simulated. Figure 25 illustrates the difference between the simulated acceleration with and without connector element relative to the experimental acceleration data.
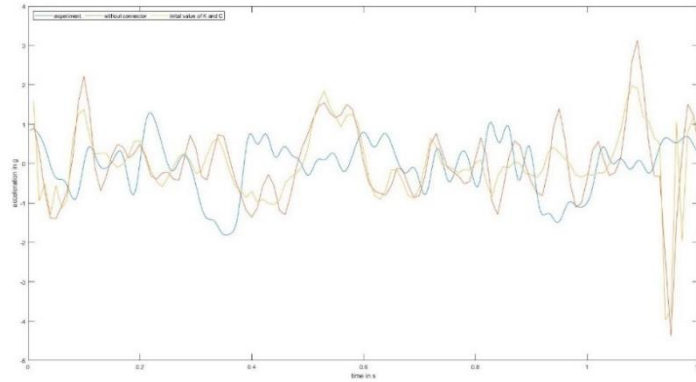

Figure 25: Simulated acceleration with connector element and without connector element to the experimental acceleration

Only the connector element in the driver and rear positions and the mass and spring damper system in the driver and rear positions are illustrated in the figure. The influence on acceleration data is analyzed based on the mass, spring, and damping coefficients.

4. Results

4.1 Critical time point analysis

For the critical point analysis, time-frequency analysis, such as Short-term Fourier Transform and Frequency domain analysis such as Fast Fourier Transform is done on the time displacement signals of the Swingarm and Steering head, with the results given in the time-frequency plots below Figure 26 (a) and (b), respectively.
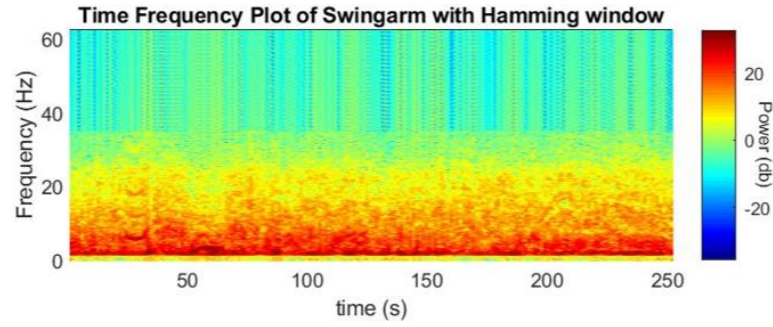
(a): Time-frequency plot of Swingarm data points
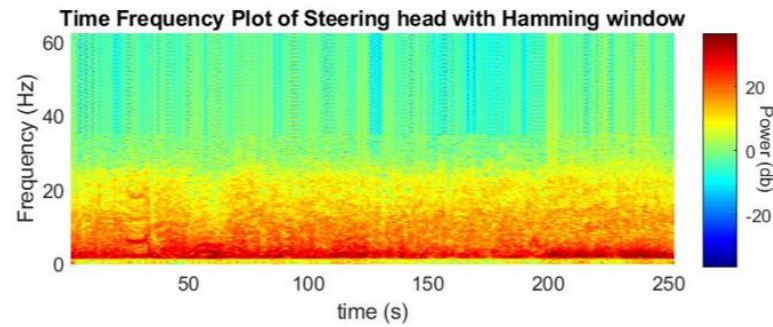
(b): Time frequency plot of Steering head points

Figure 26: Time frequency plot of (a) Swingarm, (b) Steering head signal

From Figures 26(a) and (b), it was unclear how to determine the critical areas; thus, Xspectrogram[7] analysis was done on the steering head and swingarm signals, and the findings are displayed in Figure 27.
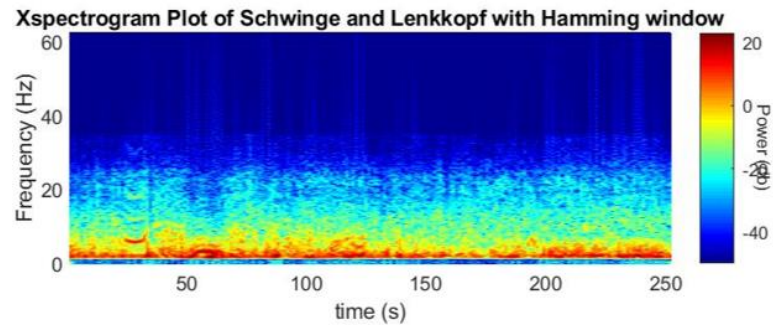

Figure 27: Xspectrogram of steering head and swingarm signal

In Figure 27, the input signals are examined using the Short-term Fourier Transform. In Figure 28(a), (b) and (c), the output of the time frequency analysis for the signal,

---

[7] Xspectrogram(x,y) is a function that provides cross-spectrogram of the signal that is specified by x and y. The input signals must be vectors with the same number of elements, and each column of s must contain an estimate of the short-term, time localized frequency content shared by x and y

including the acceleration signal from the accelerometer and strain values, are similarly evaluated and depicted.
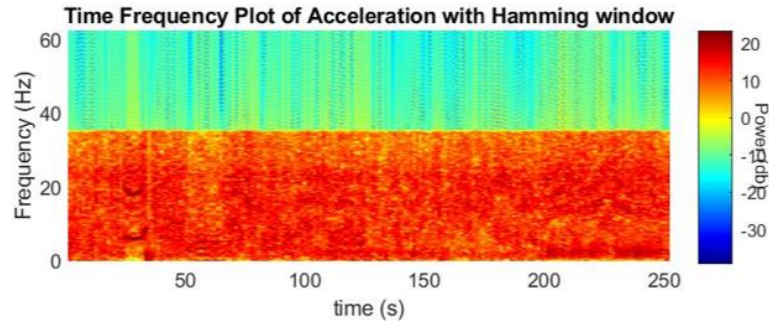
(a): Time-frequency plot of Acceleration signal
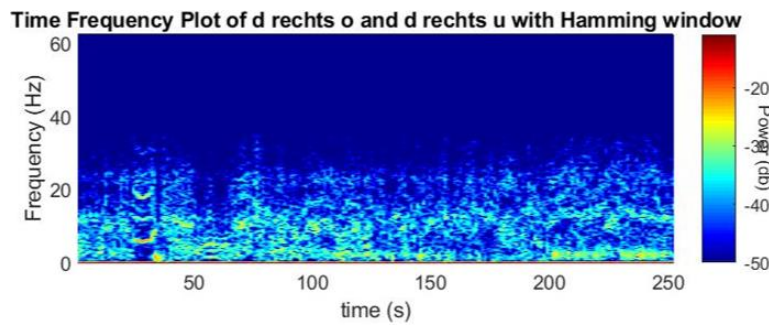
(b): Strain data from Strain gauge from the right side of the rear frame
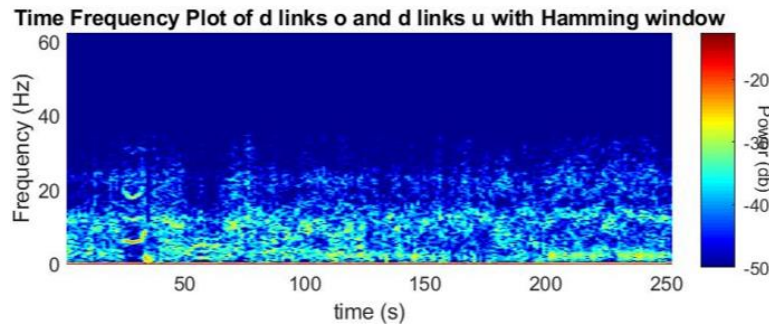
(c): Strain data from Strain gauge from the left side of the rear frame

Figure 28: (a) Time frequency plot of acceleration signal, (b) Strain data from right side of the strain gauge signal, (c) Strain data from left side of the strain gauge signal

From Figures 27, 28(a), 28(b), and 28(c) in the time-frequency plot, the critical areas identified based on the resonance pattern found in the analysis in the time points around 24-36s, 40-50s, 66-76s, 95-105s are analyzed using xspectrogram and short-term Fourier analysis in both input and output signals such as acceleration and strain data. The crucial time points are found using the time-frequency and displacement graphs. These time intervals are evaluated, and the outcomes are displayed below.

The cross-spectrogram analysis of the steering head and swing arm signal is shown in the below Figure 29(a) and similarly time-frequency analysis result for the acceleration signal is shown in Figure 29(b).
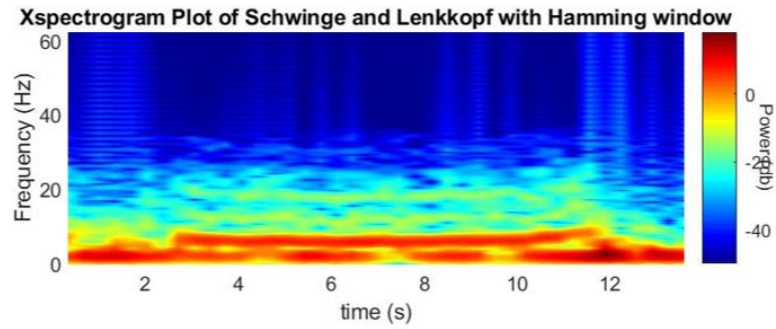
(a): Xspectrogram of Steering head and swingarm in the time segment 24-36s
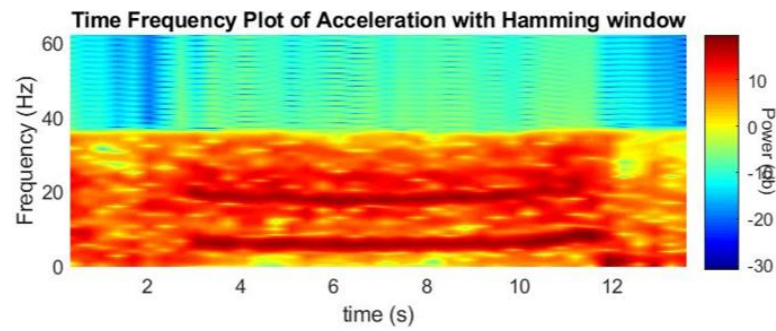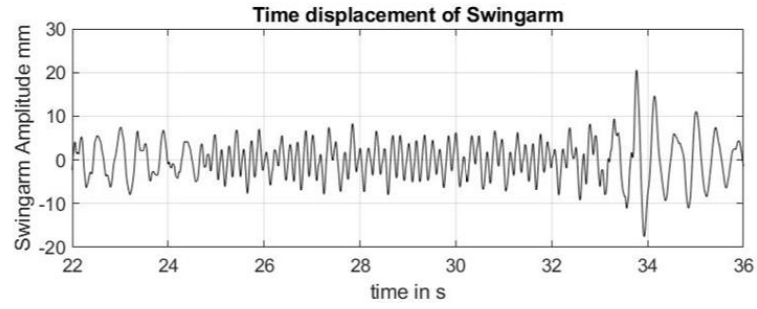

(b): Time frequency analysis of acceleration signal

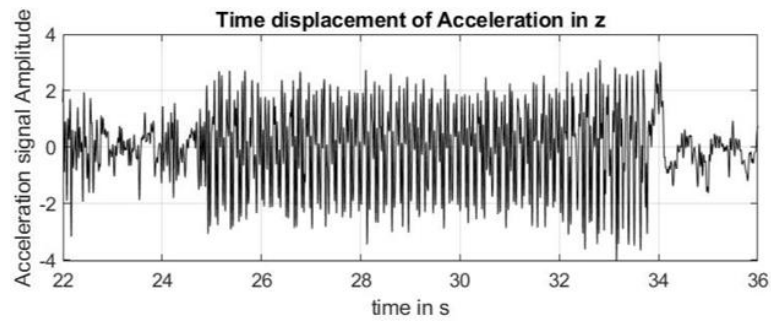Figure 29: (a) Xspectrogram of steering head and swing arm signal, (b)Time frequency plot of acceleration signal

The time displacement for the steering head, swing arm and acceleration signals are shown in Figure 30(a), (b) and (c).
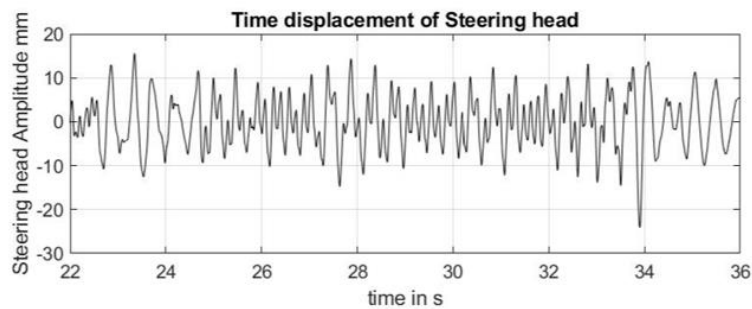
(a): Time displacement signal of Steering head

(b): Time displacement signal of Swing arm

(c): Time displacement for Acceleration signal

Figure 30: Time displacement signal of (a) Steering head, (b) Swingarm and (c) Acceleration signal

Similarly, strain gauge data points are analysed using Time-frequency analysis and Xspectrogram of the strain gauge signals are depicted in Figure 31.
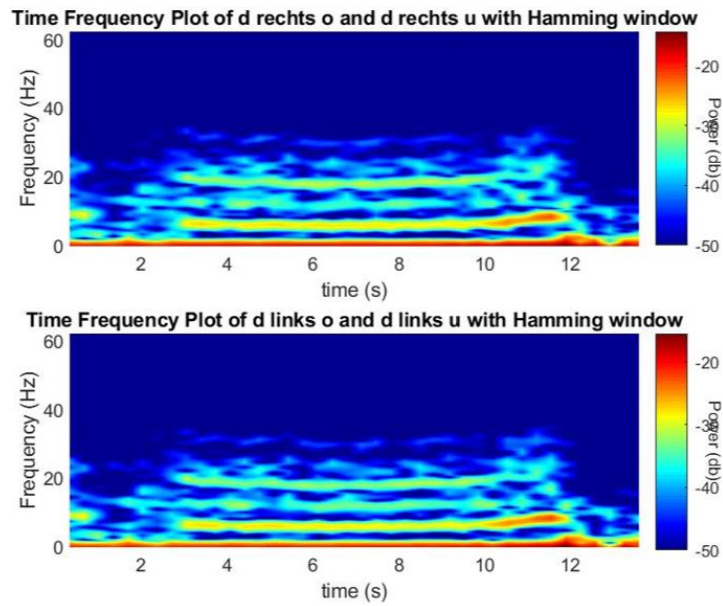
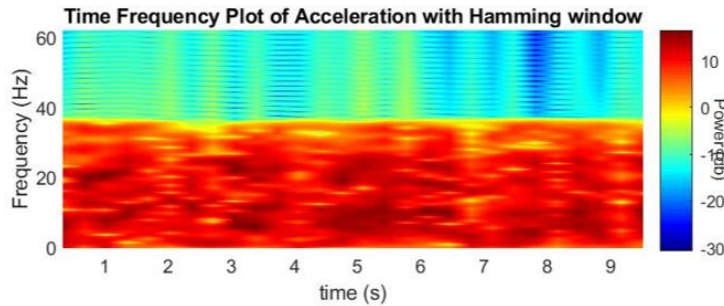Figure 31: Xspectrogram of Strain gauge signal

It is evident from Figures 29, 30, and 31 that the high amplitude Steering head and Swingarm occur at around 34s and that the accompanying acceleration signal reaches high amplitude at this time. Similarly, the Xspectrograms of the Steering head, swing arm, and acceleration signals attain their maximum power density at approximately 34s.

II. Time points between 40-50s:

Figure 32(a) depicts the cross-spectrogram analysis of the steering head and swing arm signal, while Figure 32(b) depicts the time-frequency analysis result for the acceleration signal.
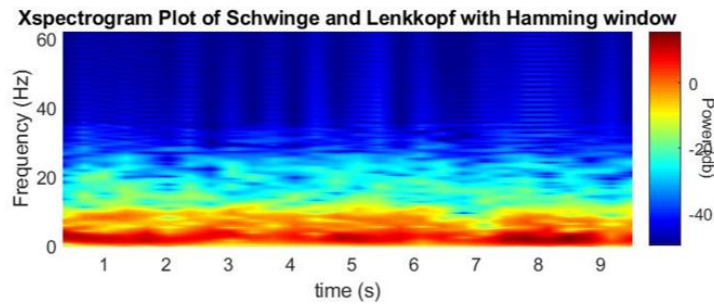
(a): Xspectrogram of Steering head and swingarm in the time segment 40-50s

(b): Time frequency analysis of acceleration signal

Figure 32: (a) Xspectrogram of steering head and swing arm signal, (b)Time frequency plot of acceleration signal

Figure 32(b) depicts the highest power density of the signal over the whole frequency range. Based on the time displacement analysis of the total signal, the crucial period point is determined. The time displacement for the steering head, swing arm and acceleration signals are shown in Figure 33(a), (b) and (c).
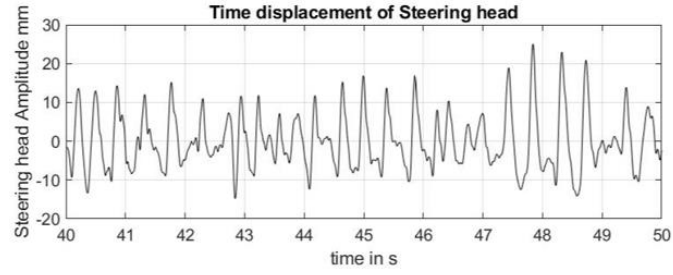
(a): Time displacement signal of Steering head
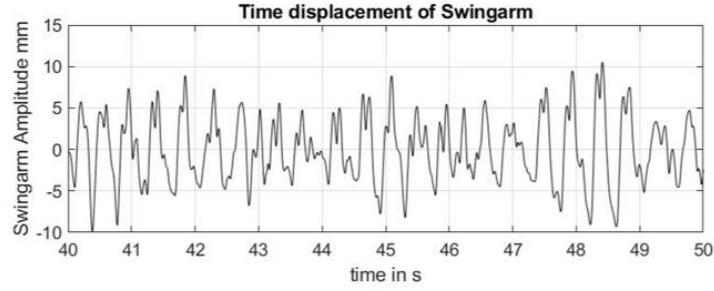
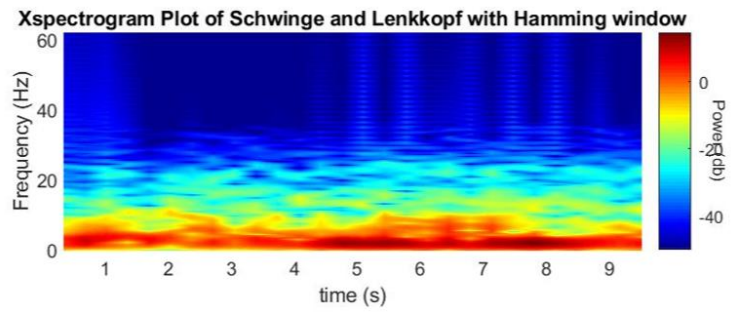(b): Time displacement signal of Swing arm
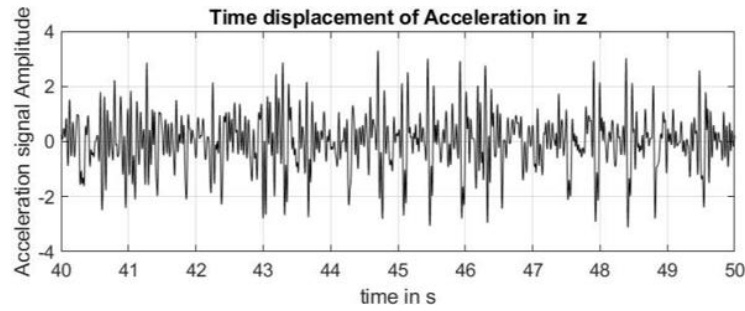
(c): Time displacement for Acceleration signal

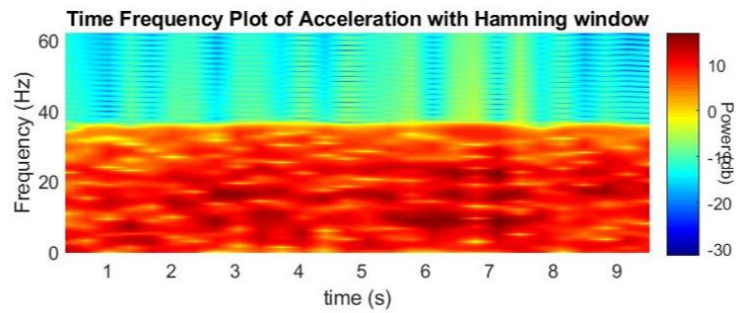Figure 33: Time displacement signal of (a) Steering head, (b) Swingarm and (c) Acceleration signal

Figures 32 and 33 reveal that the high amplitude Steering head and Swingarm occur at around 48s and that the associated acceleration signal also achieves high amplitude at this time. Likewise, the Xspectrograms of the Steering head, swing arm, and acceleration signals reach their maximum power density roughly 48s later.

III. Time points between 95-105s:

Figure 34(a) illustrates the Xspectrogram analysis of both the steering head and swingarm signal, whereas Figure 34(b) illustrates the result of the short-term Fourier Transform analysis of the acceleration signal.

(a): Xspectrogram of Steering head and swingarm in the time segment 95-105s


(b): Time frequency analysis of acceleration signal

Figure 34: (a) Xspectrogram of steering head and swing arm signal, (b)Time frequency plot of acceleration signal
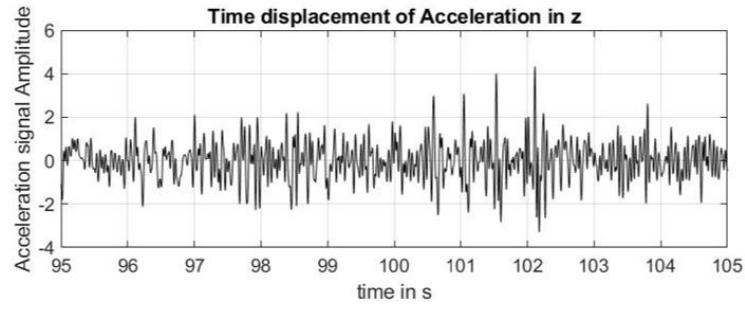
Figure 34(b) illustrates the peak signal power density of about 101-102s. Figure 35(a), (b), and (c) depict the time displacement for the steering head, swing arm, and acceleration signals, respectively
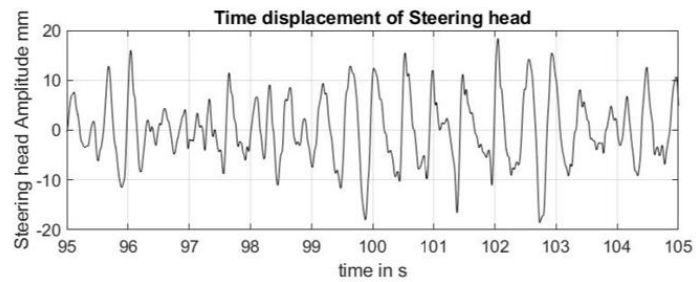
(a): Time displacement signal of Steering head
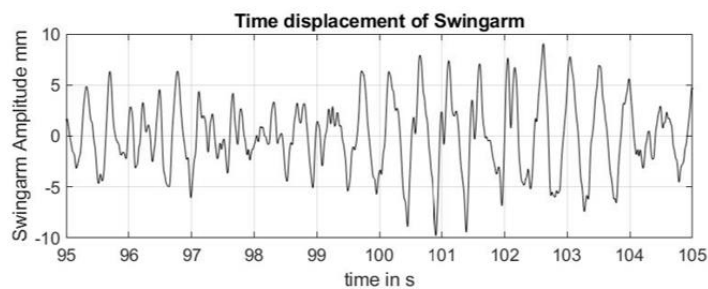
(b) Time displacement signal of Swing arm

(c) Time displacement for Acceleration signal

Figure 35: Time displacement signal of (a) Steering head, (b) Swingarm and (c) Acceleration signal

Figure 36 depicts the associated Xspectrogram of the strain gauge data examined using the Short-Time Fourier Transform.
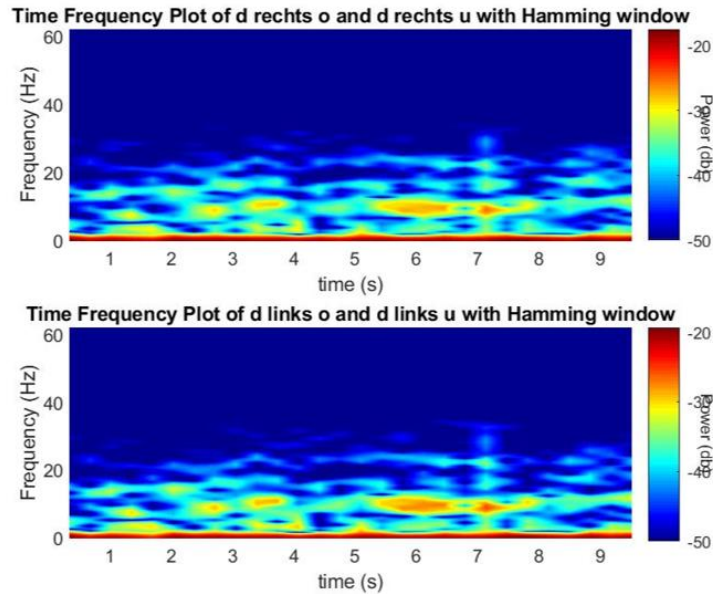

Figure 36: Xspectrogram of Strain gauge signal

Figures 35(a), (b), and (c) demonstrate that the high amplitude Steering head and Swingarm occur at around 101-102s and that the corresponding acceleration signal also attains high amplitude at this time. Similarly, the Xspectrograms of the Steering head, swing arm, and acceleration signals reach their peak power density of approximately 102s.

IV. Time points between 66-76s:

Figure 37(a) illustrates the cross-spectrogram investigation of the steering head and swingarm signal, whereas Figure 37(b) depicts the time-frequency analysis of the acceleration signal.
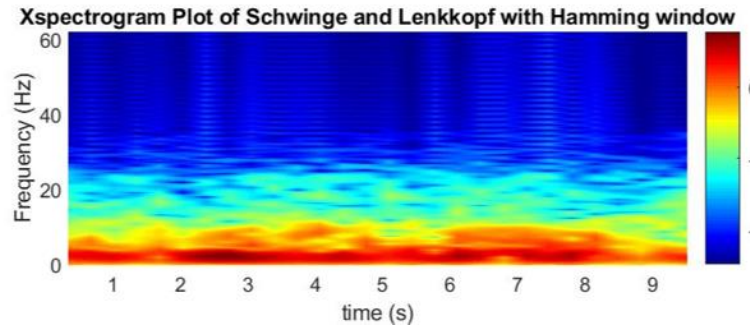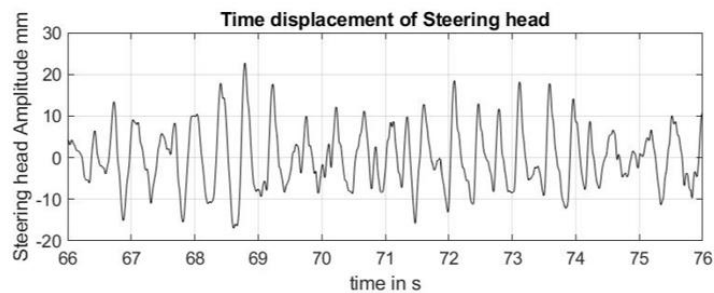

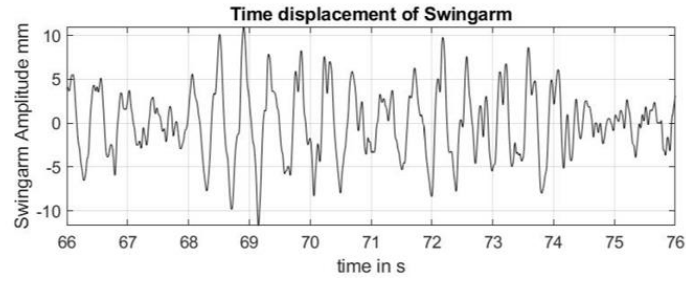(a): Xspectrogram of Steering head and swingarm in the time segment 66-76s
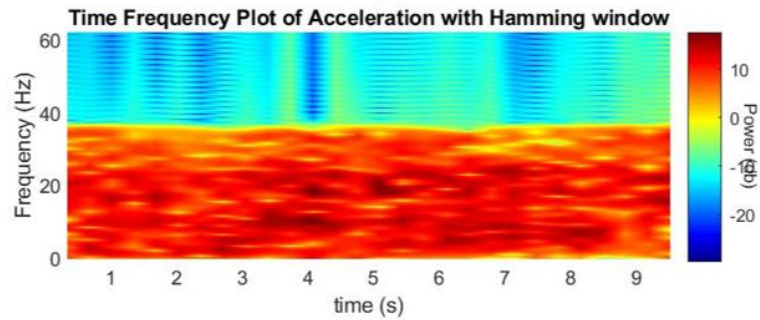
(b): Time frequency analysis of acceleration signal

Figure 37: Xspectrogram of steering head and swing arm signal, (b)Time frequency plot of acceleration signal

From Figure 37(b), it is unclear to determine the critical time period based on the time-frequency analysis of the acceleration signal. The time displacement for the steering head, swing arm and acceleration signals are shown in Figure 38(a), (b) and (c).

(a): Time displacement signal of Steering head

(b): Time displacement signal of Swing arm
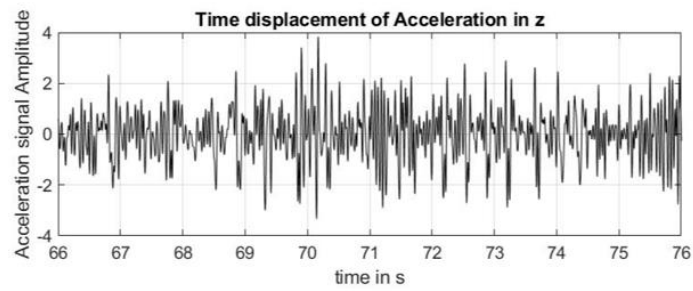
(c): Time displacement for Acceleration signal

Figure 38: Time displacement signal of (a) Steering head, (b) Swingarm and (c) Acceleration signal

Figures 37(a) and 38 demonstrate that the high amplitude Steering head and Swingarm occur at around 70s and that the corresponding acceleration signal likewise attains high amplitude. Similarly, the Xspectrograms of the steering head and Swingarm achieve their maximum power density approximately 70s later. Likewise, the strain signals are analyzed using Time-Frequency analysis, and the signal's Xspectrogram is displayed below Figure 39.
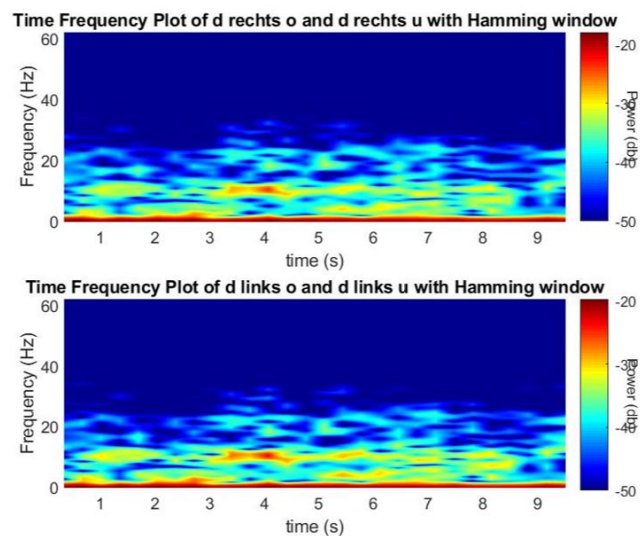

Figure 39: Xspectrogram of Strain signal

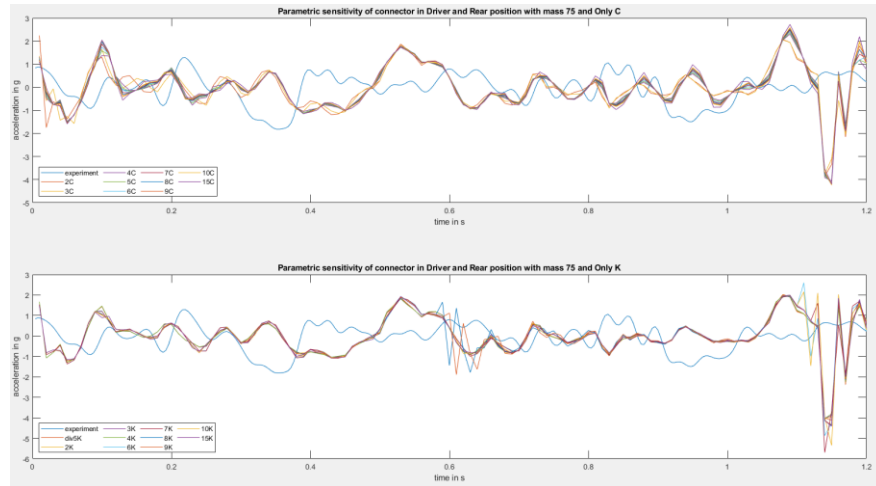## 4.2 Parametric Study with varying mass, spring and damping coefficients:

The connector elements' mass, spring, and damping coefficients are adjusted, and the impact of acceleration signals is investigated using parametric analysis. The acceleration data is compared to the experimental findings to validate the simulation results. With altering mass, spring, and damping coefficients, the results of the parametric analysis with connection element in driver and rear positions, connector in both driver, rear, and luggage carrier, and connector in all locations such as driver, rear, luggage carrier, and top-case are listed below.

I.   Connector element in driver and rear position:

The spring and damping coefficients are varied from one to ten times greater than the initial value with masses of 50kg and 75kg, respectively, and the results are presented in Figures 40 (a) and (b).
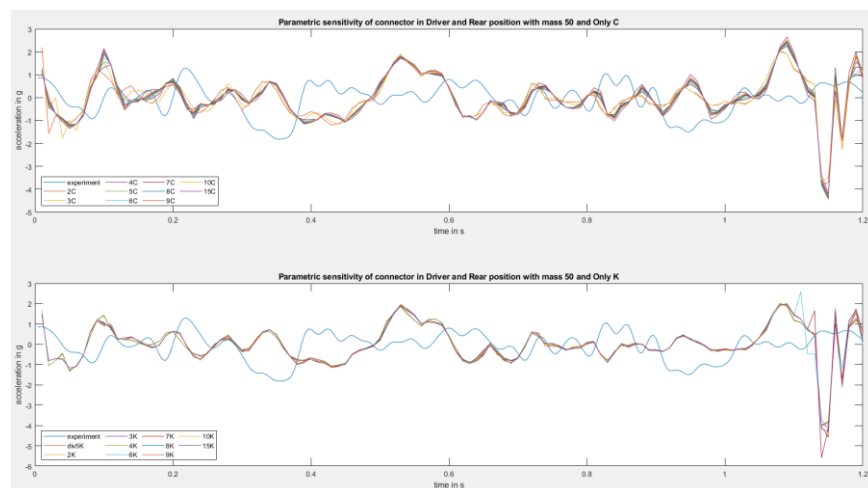
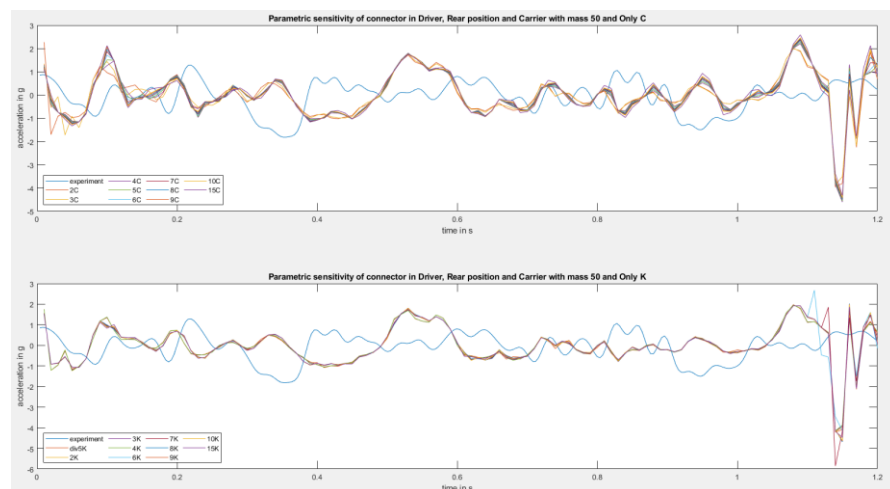(a): Mass 50 kg and varying damping, spring coefficients

(b): Mass 75 kg and varying damping, spring coefficients

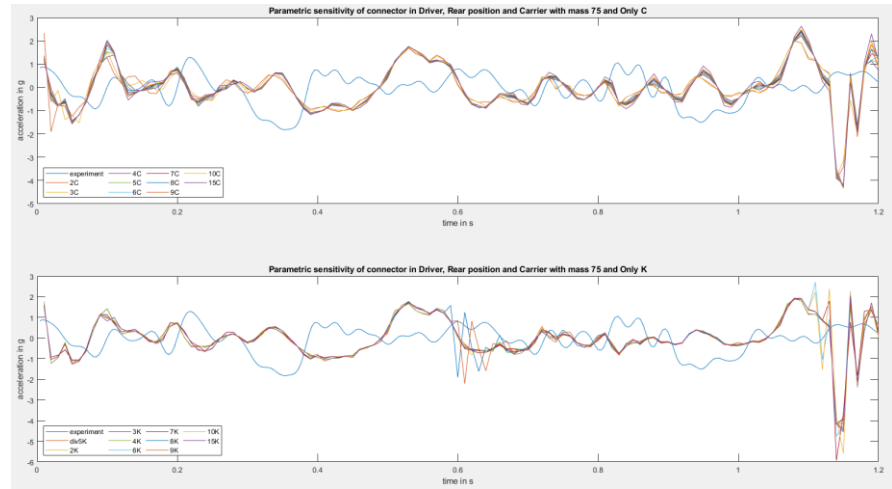Figure 40: Parametric study with (a) mass 50Kg and (b) mass 75Kg with varying damping and spring coefficients

Figures 40(a) and 40(b) show that adjusting the spring and damping coefficients does not affect the simulation acceleration data. As a result, the connector element needs to extend to the luggage carrier.

## II.   Connector in both driver, rear, and luggage carrier:

The connector element is extended to the luggage carrier in addition to the driver and rear positions. The connectors' spring and damping coefficients and the mass of 50, 75, 95, and 110 kgs were changed, and the results are presented in the below Figures.
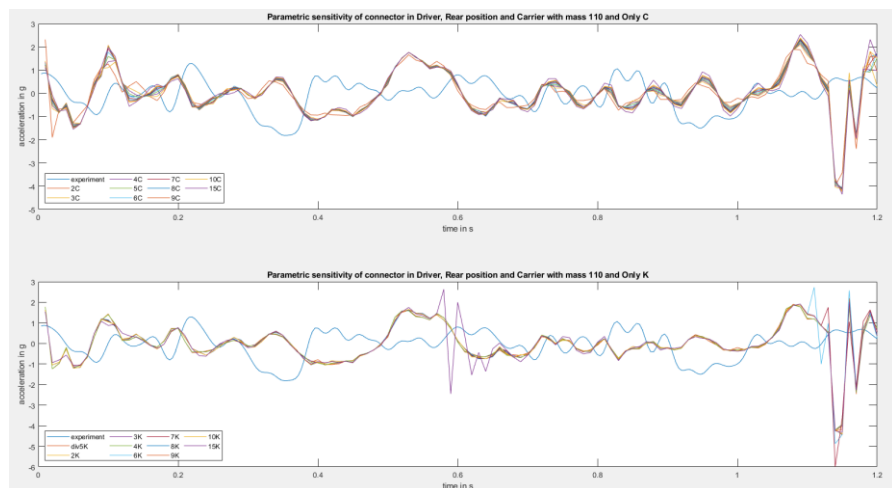

(a): Mass 50 kg and varying damping, spring coefficients

(b): Mass 75 kg and varying damping, spring coefficients
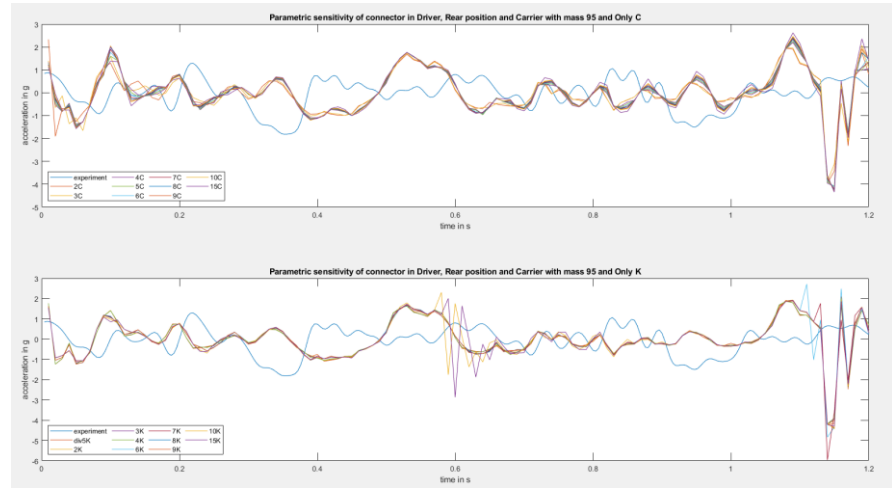
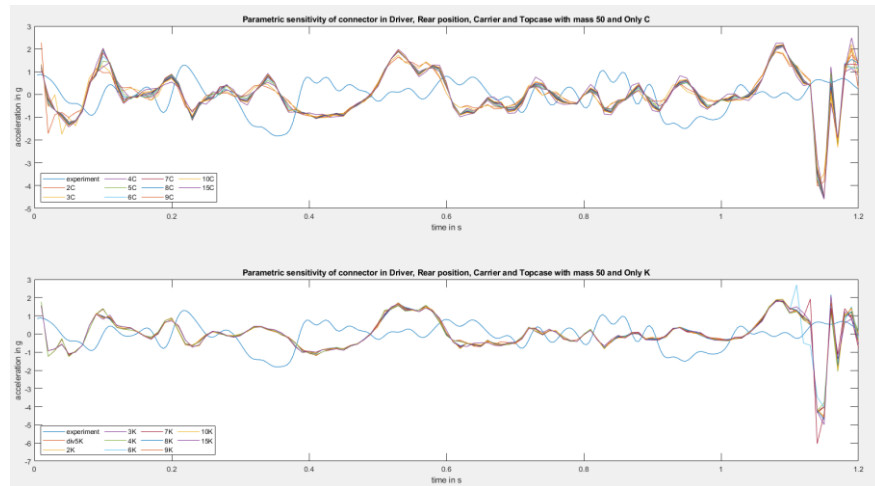(c): Mass 95 kg and varying damping, spring coefficients

(d): Mass 110 kg and varying damping, spring coefficients

Figure 41: Parametric Sensitivity analysis with (a) mass 50Kg, (b) mass 75Kg, (c) mass 95Kg and (d) mass 110Kg with varying spring and damping coefficients

The fixed mass is attached to the experimental setup's driver, rear, luggage carrier, and top case locations. The connector element is placed in the top-case position, and the parametric analysis is carried out. The acceleration signal of the simulation result changes by modifying the spring coefficients as a result of the parametric study with the connector in the driver, rear, and luggage carrier.

III.   Connector in driver, rear, luggage carrier, and top-case:

The fixed mass in the driver, rear, luggage carrier, and top-case locations is replaced by a connector element in the experimental setup. The spring and damping coefficients of the connector elements with the mass of 50, 75, 95, and 110 kg are varied, and the parametric results are shown below.
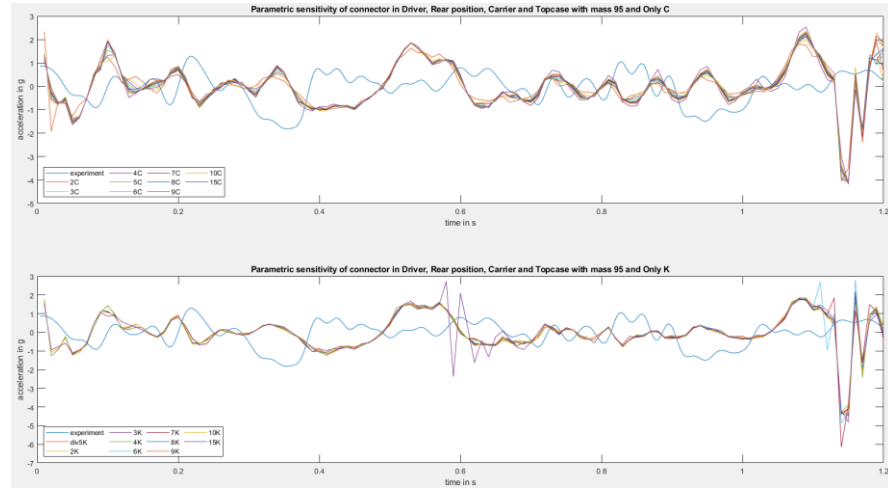

(a): Mass 50 kg and varying damping and spring coefficients
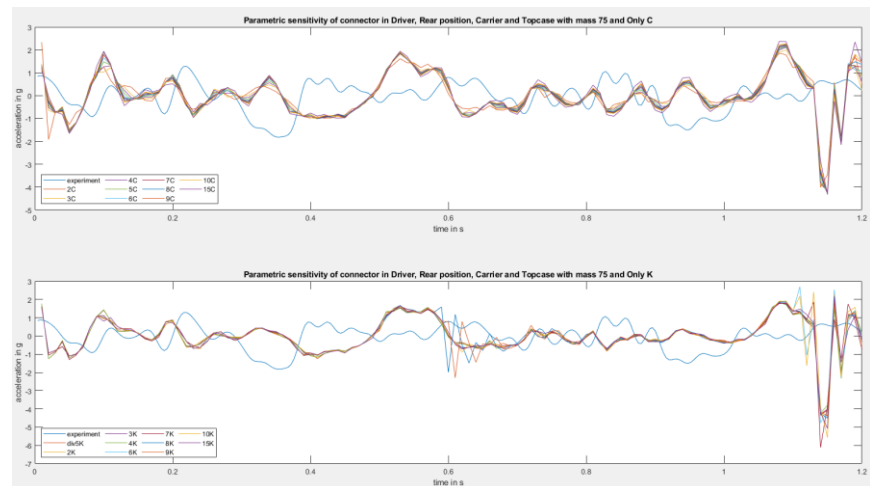
(b) Mass 75 kg and varying damping and spring coefficients
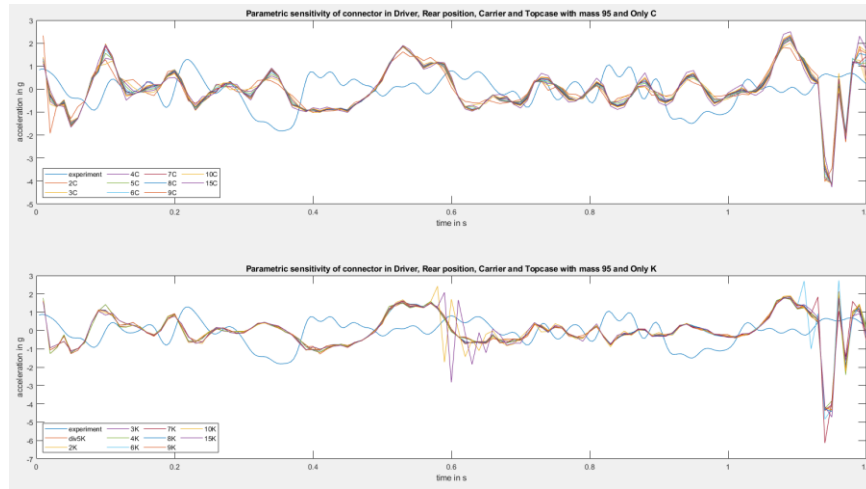
(c) Mass 95 kg and varying damping and spring coefficients

(d) Mass 110 kg and varying damping and spring coefficients

Figure 42: Parametric Sensitivity analysis with (a) mass 50Kg, (b) mass 75Kg, (c) mass 95Kg and (d) mass 110Kg with varying spring and damping coefficients

The parametric examination of the connector element with the driver, rear, luggage carrier, and top-case demonstrates that the damping coefficients have no effect on the acceleration signal from simulation. The simulation acceleration signal varies when the spring coefficients are changed.

References

Brie, D., 2000. Modelling of the spalled rolling element bearing vibration signal: an overview and some new results. *Mechanical Systems and Signal Processing,* Volume 14, pp. 353--369.

Gao, R. X. a. Y. R., 2006. Non-stationary signal processing for bearing health monitoring. *International journal of manufacturing research,* Volume 1, pp. 18--40.

Heng, R. a. N. M., 1998. Statistical analysis of sound and vibration signals for monitoring rolling element bearing condition. *Applied Acoustics,* Volume 53, pp. 211--226.

Mori, K. a. K. N. a. Y. T. a. U. Y., 1996. Prediction of spalling on a ball bearing by applying the discrete wavelet transform to vibration signals. *Wear,* Volume 195, pp. 162--168.

Statutory Declaration

"Hereby, I (we) formally declare that I (we) have developed and written the enclosed thesis without illegitimate help of a third party and that no other than the indicated aids have been used for its completion; all thoughts from other sources that have been used literally or indirectly are marked as such. The thesis has not been submitted to any other examination committee in this or a similar form."

Location:

Date and Signature:

Appendix 1